

Cascaded Dual Vision Transformer for Accurate Facial Landmark Detection

Ziqiang Dang^{1,2,*}, Jianfang Li^{2,*†}, Lin Liu²

¹Zhejiang University, ²Institute for Intelligent Computing, Alibaba Group

Abstract

Facial landmark detection is a fundamental problem in computer vision for many downstream applications. This paper introduces a new facial landmark detector based on vision transformers, which consists of two unique designs: Dual Vision Transformer (D-ViT) and Long Skip Connections (LSC). Based on the observation that the channel dimension of feature maps essentially represents the linear bases of the heatmap space, we propose learning the interconnections between these linear bases to model the inherent geometric relations among landmarks via channel-split ViT. We integrate such channel-split ViT into the standard vision transformer (i.e., spatial-split ViT), forming our Dual Vision Transformer to constitute the prediction blocks. We also suggest using long skip connections to deliver low-level image features to all prediction blocks, thereby preventing useful information from being discarded by intermediate supervision. Extensive experiments are conducted to evaluate the performance of our proposal on the widely used benchmarks, i.e., WFLW [45], COFW [3], and 300W [34], demonstrating that our model outperforms the previous SOTAs across all three benchmarks.

1. Introduction

Facial landmark detection involves locating a set of pre-defined key points on face images, serving as a fundamental step for supporting various high-level applications, including face alignment [14, 19, 47, 47], face recognition [43, 51, 56], face parsing [36] and 3D face reconstruction [5, 8, 22].

Early approaches of landmark detection relied on statistical models [4, 11], but have been surpassed by modern landmark detectors that use convolutional neural networks (i.e., CNN) [38, 53, 55]. CNNs learn a transformation between image features and a set of 2D coordinates or regress heatmaps to represent the probability distribution of landmarks. Besides, these detectors [6, 18, 21, 44, 54] usually employ cascaded networks in conjunction with in-

termediate supervision to progressively refine the predictions, producing remarkable advances. To capture the intrinsic geometric relationships among landmarks for accurate predictions, researchers have also developed various effective methods using Graph Convolutional Networks (GCNs) [24, 25], Graph Attention Networks (GATs) [31] or Transformers [23, 46, 49]. However, these methods primarily utilize patch-based image features to learn spatial relations among landmarks.

In this paper, we have developed a vision transformer-based model architecture and modeled the intrinsic geometric relationships among landmarks by computing the correlations between the linear bases of heatmap space, enabling us to achieve new SOTA results across all three benchmarks. Following the design paradigm of cascaded networks [6, 18, 21, 44, 54], we repeat prediction blocks in conjunction with intermediate supervisions. Specially, in our architecture, we propose two unique designs: Dual Vision Transformer (D-ViT), which constitutes the prediction blocks, and Long Skip Connections (LSC), the strategy for connecting these blocks.

The standard vision transformer [10] discretizes images or feature maps into small patches, then rearranges them into a sequence to extract global and local image features. However, it lacks the ability to model the underlying geometric characteristics of landmarks. To address this, we propose incorporating the channel-split ViT to model the inherent relationships among landmarks. Specifically, the prediction block outputs a feature map $F \in \mathbb{R}^{C \times H \times W}$ for intermediate supervision, which can be split along the channels into $F = (f_1, f_2, \dots, f_C)$. Therefore, when considering using convolution operations to regress the feature map F into the heatmaps, the heatmap for each landmark is actually a linear combination of f_m . To put it another way, the channel dimension of feature maps essentially represents the linear bases of the heatmap space. Based on such insight, we take advantage of the transformer architecture to learn underlying relationships among these linear bases, allowing for adaptive computation of their interconnections through the multi-head self-attention mechanism. Finally, the spatial-split ViT and the channel-split ViT together form our Dual Vision Transformer (D-ViT).

*Ziqiang Dang and Jianfang Li contributed equally to this work.

†Corresponding author: Jianfang Li, wuhui.ljf@alibaba-inc.com.

Following the classic stacked Hourglasses networks [18, 29, 44, 54], which utilize residual connections between two sequential hourglass architectures, we first also apply the same connection strategy to boost the network. However, we find that when the number of prediction blocks exceeds 4, the detection performance is instead diminished by deeper model architecture. As far as we know, this is caused by intermediate supervisions, which can lead to the inadvertent discard of useful information. To handle this problem, we suggest using long skip connections to deliver low-level image features to all prediction blocks, thereby making deeper network architectures feasible.

We evaluate the performance of our proposal on the widely used benchmarks, *i.e.*, WFLW [45], COFW [3], and 300W [34]. Extensive experiments demonstrate that our approach outperforms the previous state-of-the-art methods and achieves a new SOTA across all three datasets. The main contributions can be summarized as follows:

1) We introduce a facial landmark detector based on our unique dual vision transformer (D-ViT), which is able to effectively capture contextual image features and underlying geometric relations among landmarks via spatial-split and channel-split features.

2) To avoid losing useful information due to intermediate supervision and make deeper network architectures feasible, we propose a unique connection strategy, *i.e.*, Long Skip Connections, to transmit low-level image features from ResNet to each prediction block.

3) Extensive experiments are conducted to evaluate our approach, demonstrating its good generalization ability and superior performance compared to existing SOTAs across three publicly available datasets (*i.e.*, WFLW, COFW, and 300W). Our code will be released for reproduction.

2. Related Work

In the literature on facial landmark detection, deep learning methods can generally be divided into two categories: coordinate regression-based method and heatmap-based method.

Coordinate regression-based methods directly regress facial landmarks through learning the transformation between image features and landmark coordinates. These methods [6, 27, 38, 40, 53, 55] are typically designed in a coarse-to-fine manner, employing multiple prediction stages or cascaded network modules to gradually refine the landmark coordinates. In these methods, ResNet [15] combined with wing loss [12] is commonly used as the backbone to extract image features and regress landmark coordinates. DTLD [23] adopts pretrained ResNet [15] to extract multi-scale image features and apply cascaded transformers to gradually refine landmarks by predicting offsets. Considering the underlying geometric relationships among landmarks, SDL [24] and SDFL [25] utilize graph convo-

lutional networks to explicitly capture structural features. Besides, SLPT [46] introduces a sparse local patch transformer to learn the intrinsic landmark relations, which extracts the representation (*i.e.*, embedding) of each individual landmark from the corresponding local image patch and processes them based on the attention mechanism.

Heatmap-based methods [7, 9, 29] predict a heatmap for each landmark, where the point with the highest intensity, or its vicinity, is considered the optimal position of the landmark. In these methods, UNet [33] and the stacked hourglasses network [29] are frequently used as backbone architectures. HRNet [37, 42] showed remarkable results through the combination of multi-scale image features. Adaptive wing loss [44] was proposed as the loss function for heatmap regression to balance the normal and hard cases. Besides, the predictions can be further improved by integrating coordinate encoding with CoordConv [26]. However, heatmap-based methods usually suffer from discretization-induced errors, since the heatmap size is usually much smaller than the input image. Consequently, various methods have been developed to alleviate discretization-induced errors, including the usage of heatmap matching to improve accuracy [39], continuous heatmap encoding and decoding method [2], differential spatial to numerical transform (DSNT) [30] and Heatmap in Heatmap (HIH) [21] for subpixel coordinates. Additionally, LAB [45] suggests predicting the facial boundary as a geometric constraint to help regress the landmark coordinates. LUVL [20] predicts not only the landmark positions but also the uncertainty and probability of visibility for better performance. SPIGA [31] combines CNN with cascaded Graph Attention Networks to jointly predict head pose and facial landmarks. ADNet [18] introduces anisotropic direction loss (ADL) and anisotropic attention module (AAM) to address ambiguous landmark labeling. STARLoss [54] adaptively suppresses the prediction error in the first principal component direction to mitigate the impact of ambiguity annotation during the training phase. LDEQ [28] employs Deep Equilibrium Models [1] to detect face landmarks and achieves state-of-the-art results on the WFLW benchmark [45]. Recently, FRA [13] learned a general self-supervised facial representation for various facial analysis tasks, achieving state-of-the-art results on the 300W benchmark [34] among self-supervised learning methods for facial landmark detection. Most of these methods utilize convolutional neural networks and produce remarkable results. In this work, we have developed a vision transformer-based model architecture and achieved new SOTA results across all three benchmarks.

3. Method

The architecture of our proposed model is presented in Fig. 1, which utilizes ResNet [15] to extract low-level im-

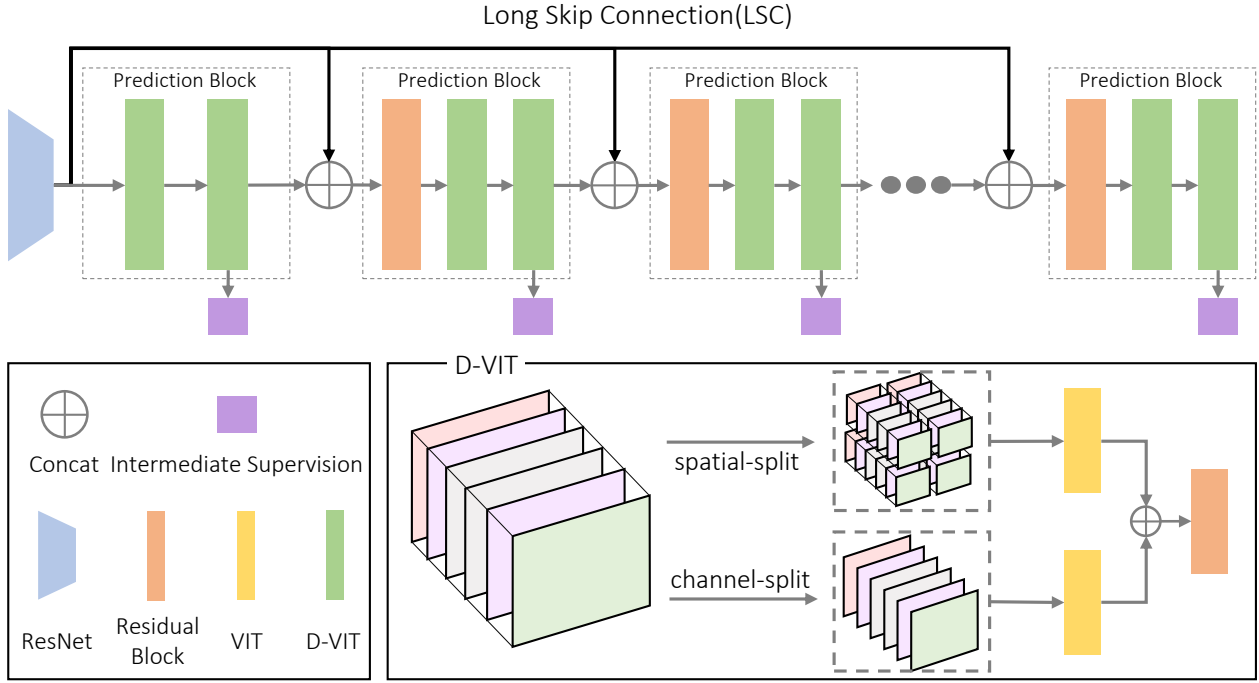


Figure 1. Architecture of our framework. Long skip connections (depicted as upper black lines) distribute low-level features to each prediction block, thereby preventing useful information from being discarded by intermediate supervision. D-ViT learns contextual features of the image through spatially split patches and captures the underlying geometric relations among landmarks using channel-split features.

age features and employs repeated prediction blocks in conjunction with intermediate supervision to gradually improve the detection performance. We will describe the core design of our architecture, Dual Vision Transformer and Long Skip Connection, in Sec. 3.1 and Sec. 3.2, respectively, and then introduce the training loss in Sec. 3.3.

3.1. Dual Vision Transformer

Our dual vision transformer (D-ViT) is built upon the standard vision transformer (ViT) [10], which discretizes the input image or feature map into smaller spatial patches and arranges these patches into a sequence. Then, the attention mechanism is utilized to establish relationships among the patches, allowing for the extraction of both local and global image features. However, the standard ViT does not explicitly leverage the geometric relationships among landmarks. Consequently, we propose to incorporate a channel-split ViT to establish the relationships between bases in the heatmap space, thereby extracting the underlying geometric features among landmarks. The proposed channel-split ViT can be seamlessly integrated into the ViT architecture without the need for extra steps, such as explicit conversion to the heatmaps or landmark coordinates. Finally, the spatial-split ViT and the channel-split ViT together form our Dual Vision Transformer (D-ViT), as shown in Fig. 1.

The design of the channel-split ViT is based on the in-

sight that the channel dimension of feature maps essentially represents the bases of the heatmap space. Specifically, in the architecture, the prediction block outputs a feature map $F \in \mathbb{R}^{C \times H \times W}$ for intermediate supervision, where C , H and W denote the number of channels, height, and width. Then, the feature map F can be split along the channels into $F = (f_1, f_2, \dots, f_C)$, where $f_m \in \mathbb{R}^{H \times W}$. Therefore, when considering using convolution operations to regress the feature map F into the heatmaps, the heatmap for each landmark in the intermediate supervision is actually a linear combination of f_m :

$$h_i = \sum_{m=1}^C \alpha_m^i f_m, \quad (i = 1, 2, \dots, M), \quad (1)$$

where M is the number of landmarks, h_i is the heatmap of i -th landmark, and α_m^i is learnable parameters. In experiment, such linear combination can be implemented using a Conv2D layer with 1×1 kernel. Besides, Fig. 2 presents a visual explanation.

Eq. (1) and Fig. 2 show that the separated sub feature maps (f_1, f_2, \dots, f_C) are actually linear bases of the heatmap space. Since the heatmaps determine the coordinates of the landmarks, we can capture the inherent geometric relations among landmarks by analyzing the relations among the linear bases of heatmap space.

In our implementation, we utilize transformer to capture

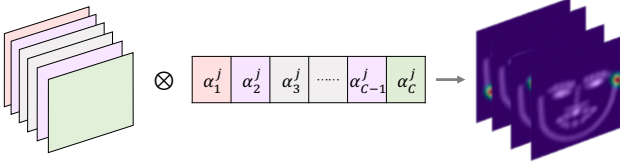


Figure 2. Heatmap is linear combination of channel-split features. \otimes denotes dot-product. Intermediate supervision uses Conv2D with 1×1 kernel to convert the features extracted from a prediction block into heatmaps. This implies channel-split features linearly expand the heatmap space. Based on this observation, we take advantage of the self-attention mechanism to learn underlying geometric relations among landmarks via channel-split features.

the inherent relationships among the linear bases (f_1, f_2, \dots, f_C), allowing for adaptive computation of their interconnections through the multi-head self-attention mechanism, which is the core component of the transformer architecture [41]. For self-containedness, we briefly describe the self-attention mechanism. It projects an input sequence $X \in \mathbb{R}^{L \times d}$ into query $Q \in \mathbb{R}^{L \times d}$, key $K \in \mathbb{R}^{L \times d}$, and value $V \in \mathbb{R}^{L \times d}$ by three learnable matrices. The attention mechanism is formulated as follows:

$$\text{Attention}(Q, K, V) = \text{softmax}\left(\frac{QK^T}{\sqrt{d}}\right)V. \quad (2)$$

Then, our D-ViT is formally defined as:

$$\text{D-ViT} = \text{Conv}(\text{ViT}(\text{Pat}) \parallel \text{ViT}(\text{Chn})), \quad (3)$$

where Pat denotes the spatial-split patches, Chn represents the channel-split features, \parallel refers to concatenation along the channel dimension and $\text{Conv}(\cdot)$ is a residual convolution block. Beneficial from such design, our D-ViT can leverage both spatial-split patches and channel-split features to extract image features and establish inherent relations among landmarks, thereby achieving new state-of-the-art results across three benchmarks. In the following discussion, we refer to the standard ViT with spatially split patches as spatial-split ViT, and the ViT with channel-split features as channel-split ViT.

3.2. Long Skip Connection

Following the design paradigm of the widely used hour-glasses networks [29, 52], which often serve as backbones for facial landmark detection [18, 21, 29, 44, 54], we repeat the prediction block in conjunction with intermediate supervision to consolidate feature processing. However, we found that when using residual connections between two sequential prediction blocks (*i.e.*, ResCBSP in Fig. 5a), the detection performance is instead diminished by deeper prediction blocks. More details can be found in the ablation study in Sec. 4.3.

The reason of this behavior is the supervision of outputs from intermediate prediction blocks. Specifically, during training, supervision at all intermediate stages compels the network to extract relevant information for estimating landmarks. However, this can also lead to the loss of some information; since shallow prediction blocks may not perform optimally, they might inadvertently discard useful information that could be better processed by deeper prediction blocks.

Therefore, unlike previous methods that use residual connections between two consecutive prediction blocks, we propose using long skip connections (LSC) to distribute low-level image features, thereby making deeper network architectures feasible. Specifically, the LSC (shown as the upper black line in Fig. 1) originates from the low-level image features extracted by ResNet and transmits these features to each prediction block. As a result, each intermediate prediction block receives features extracted from the previous block as well as the complete low-level features.

3.3. Training Loss

We adopt the widely used soft-argmax operator to decode heatmaps into landmark positions. Let h_i^j denote the heatmap for the i -th landmark predicted by j -th intermediate supervision. We denote the k -th pixel position in the heatmap as g_k and the heatmap value at g_k as h_{ik}^j . The corresponding landmark location for heatmap h_i^j is given by:

$$\mu_i^j = \sum_{k=1}^{H \times W} h_{ik}^j g_k. \quad (4)$$

The loss for the j -th intermediate supervision consists of two components: one for supervising landmark coordinates and the other for supervising the heatmaps, as shown in the following formula:

$$\mathcal{L}_j = \sum_i (d_1(\mu_i^j, y_i) + \beta d_2(h_i^j, z_i)), \quad (5)$$

where y_i is the ground truth location of the i -th landmark, and z_i is the corresponding heatmap defined by a Gaussian kernel. β is a balance weight between coordinate and heatmap regression. d_1 and d_2 are loss functions for regressing coordinates and heatmaps. In this paper, we utilize smooth-L1 as d_1 and awing loss [44] as d_2 .

The total loss for optimizing our network is a combination of the loss terms from each intermediate supervision:

$$\mathcal{L}_{\text{total}} = \sum_{j=1}^B w^{j-B} \mathcal{L}_j, \quad (6)$$

where B is the number of prediction blocks, and $w (w \geq 1)$ is an expanding factor that balances intermediate supervisions across different block outputs.

4. Experiments

In this section, we first introduce the experimental setup, including the datasets, evaluation metrics, and the implementation details in Section 4.1. Then, we compare our approach with state-of-the-art face landmark detection methods in Section 4.2. Finally, we perform ablation studies to analyze the design of our framework in Section 4.3.

4.1. Experimental Setup

Datasets. For experimental evaluation, we consider three widely used datasets: **WFLW** [45], **COFW** [3], and **300W** [34]. Additionally, in the ablation experiments, we also employed a video-based dataset **WFLW-V** [28] for cross-dataset validation. The WFLW dataset is based on the WIDER dataset [48] and includes 7,500 training images and 2,500 test images, each with 98 labeled keypoints. The test set is further divided into six subsets: large-pose, expression, illumination, makeup, occlusion and blur, to assess algorithm performance under various conditions. For this dataset, we use the pre-cropped WFLW dataset from Lan *et al.* [21] in our experiments. The COFW dataset features heavy occlusions and a wide range of head poses, comprising 1,345 training images and 507 test images. Each face is annotated with 29 landmarks. 300W dataset is a widely adopted dataset for face alignment and contains 3,148 images for training and 689 images for testing. The test set is divided into two subsets: common and challenge. All images are labeled with 68 landmarks. The WFLW-V dataset provides 1,000 videos, which are equally categorized into easy and hard subsets. In the cross-dataset validation, we train our model on the WFLW dataset and test it on every video frame from WFLW-V dataset.

Evaluation Metrics. For quantitative evaluation, three commonly used metrics are adopted: Normalized Mean Error (NME), Failure Rate (FR), and Area Under Curve (AUC). To calculate NME, we use the interocular distance for normalization in the WFLW and 300W datasets, and the interpupils distance for normalization in the COFW dataset. Same with previous works like STAR [54] and LDEQ [28], we report FR and AUC for the WFLW dataset with the cut-off threshold 10%. For NME and FR, lower values indicate better performance, while for AUC, a higher value is preferable.

Implementation Details. For the images fed into our network, the face regions are cropped and resized to 256×256 . Common image augmentations have been applied including random rotation, random translation, random occlusion, random blur, random color jitter, random horizontal flip, and random grayscale conversion. In our network, ResNet [15] is utilized to extract low-level image features. The ResNet in our model is built with bottleneck structure, and its number of parameters is about 13% of the standard ResNet50. We stack 8 prediction blocks to sequentially pre-

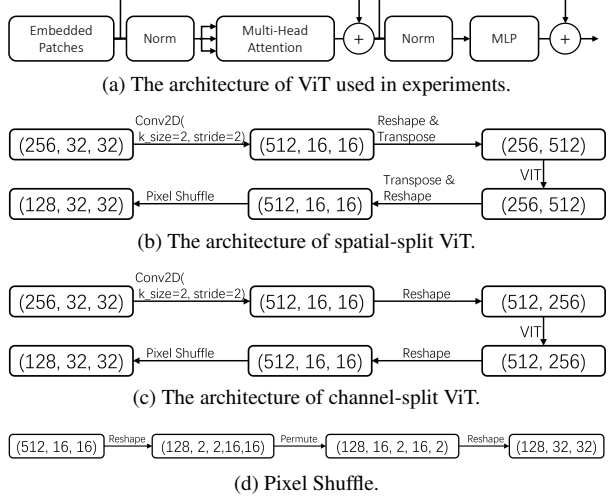


Figure 3. Implementation details of our D-ViT.

dict $256 \times 32 \times 32$ feature maps for intermediate supervision. In spatial-split ViT, we apply a Conv2d layer for patch embedding. In channel-split ViT, we use another Conv2d layer to halve the spatial size to save memory. At the end of channel-split or spatial-split ViT, pixel shuffle [35] is used to restore the spatial dimensions to 32×32 . More implementation details about D-ViT are shown in Fig. 3. Ground-truth heatmaps are generated by the 2-dimensional Gaussian distribution with small variance [50]. We employ the Adam optimizer with initial learning rate 1×10^{-4} . The learning rate is reduced by half for every 200 epochs, and we optimize the network parameters for a total of 500 epochs. The model is trained on two GPUs (Nvidia V100 16G), with a batch size of 16 per GPU.

4.2. Comparison on Detection Accuracy

In this section, we compare our method with previous state-of-the-art baselines. The NME across three datasets are reported in Tab. 1, while the FR and AUC for WFLW dataset are shown in Tab. 2. The results presented in both tables demonstrate that our approach surpasses the previous baselines and achieves a new SOTA across all three datasets.

Compared to other transformer-based methods [23, 46], our approach achieves an improvement of 0.33 and 0.37 in NME on the full WFLW dataset over DTLD [23] and SLPT [46], respectively. This demonstrates that our proposed D-ViT and long skip connection have a positive impact on the performance of transformers. Additionally, our proposal also outperforms recent CNN-based methods [28, 54] that achieved state-of-the-art results. Specifically, our NME score is 0.27 and 0.17 better than that of STAR [54] and LDEQ [28] on the full WFLW test set. Furthermore, for the Pose and Occlusion subsets, which contain severe occlusions, our method significantly improves the detection performance, demonstrating that our network

Method		WFLW						COFW		300W		
		Full	Pose	Expr.	Illum.	Makeup	Occl.	Blur	Full	Full	Comm.	Chal.
LAB [45]	CVPR'18	5.27	10.24	5.51	5.23	5.15	6.79	6.32	-	3.49	2.98	5.19
Wing [12]	CVPR'18	4.99	8.43	5.21	4.88	5.26	6.21	5.81	5.44	-	-	-
DecaFA [6]	ICCV'19	4.62	8.11	4.65	4.41	4.63	5.74	5.38	-	3.39	2.93	5.26
HRNet [37]	CVPR'19	4.60	7.94	4.85	4.55	4.29	5.44	5.42	-	3.32	2.87	5.15
AS [32]	ICCV'19	4.39	8.42	4.68	4.24	4.37	5.60	4.86	-	3.86	3.21	6.46
LUVLI [20]	CVPR'20	4.37	7.56	4.77	4.30	4.33	5.29	4.94	-	3.23	2.76	5.16
AWing [44]	ICCV'19	4.36	7.38	4.58	4.32	4.27	5.19	4.96	4.94	3.07	2.72	4.52
SDL [24]	ECCV'20	4.21	7.36	4.49	4.12	4.05	4.98	4.82	-	3.04	2.62	4.77
ADNet [18]	ICCV'21	4.14	6.96	4.38	4.09	4.05	5.06	4.79	4.68	2.93	2.53	4.58
SLPT [46]	CVPR'22	4.12	6.99	4.37	4.02	4.03	5.01	4.79	4.79	3.17	2.75	4.90
HIH [21]	ICCVW'21	4.08	6.87	4.06	4.34	3.85	4.85	4.66	4.63	3.09	2.65	4.89
DTLD [23]	CVPR'22	4.08	-	-	-	-	-	-	-	2.96	2.59	4.50
SPIGA [31]	BMVC'22	4.06	7.14	4.46	4.00	3.81	4.95	4.65	-	-	-	-
STAR [54]	CVPR'23	4.02	6.79	4.27	3.97	3.84	4.80	4.58	4.62	2.87	2.52	4.32
LDEQ [28]	CVPR'23	3.92	6.86	3.94	4.17	3.75	4.77	4.59	-	-	-	-
FRA [13]	CVPR'24	4.11	-	-	-	-	-	-	-	2.91	2.60	4.46
Ours	-	3.75	6.43	3.85	4.06	3.57	4.47	4.37	4.13	2.85	2.43	4.56

Table 1. Quantitative comparison with previous state-of-the-art methods on three public datasets using the NME metric. The **best** and **second** best results are marked in colors of red and blue, respectively. It can be seen that our method achieves new SOTA results on the full test sets of all three datasets.

Method	FR ₁₀ (↓)							AUC ₁₀ (↑)						
	Full	Pose	Exp.	Ill.	Mu.	Occ.	Blur	Full	Pose	Exp.	Ill.	Mu.	Occ.	Blur
LAB [45]	7.56	28.83	6.37	6.73	7.77	13.72	10.74	53.2	23.5	49.5	54.3	53.9	44.9	46.3
HRNet [37]	4.64	23.01	3.5	4.72	2.43	8.29	6.34	52.4	25.1	51	53.3	54.5	45.9	45.2
AS [32]	4.08	18.1	4.46	2.72	4.37	7.74	4.4	59.1	31.1	54.9	60.9	58.1	51.6	55.1
LUVLI [20]	3.12	15.95	3.18	2.15	3.4	6.39	3.23	55.7	31	54.9	58.4	58.8	50.5	52.5
AWing [44]	2.84	13.5	2.23	2.58	2.91	5.98	3.75	57.2	31.2	51.5	57.8	57.2	50.2	51.2
SDL [24]	3.04	15.95	2.86	2.72	1.45	5.29	4.01	58.9	31.5	56.6	59.5	60.4	52.4	53.3
ADNet [18]	2.72	12.72	2.15	2.44	1.94	5.79	3.54	60.2	34.4	52.3	58	60.1	53	54.8
SLPT [46]	2.72	11.96	1.59	2.15	1.94	5.7	3.88	59.6	34.9	57.3	60.3	60.8	52	53.7
HIH [21]	2.6	12.88	1.27	2.43	1.45	5.16	3.1	60.5	35.8	60.1	61.3	61.8	53.9	56.1
FRA [13]	2.53	-	-	-	-	-	-	59.1	-	-	-	-	-	-
SPIGA [31]	2.08	11.66	2.23	1.58	1.46	4.48	2.20	60.6	35.3	58	61.3	62.2	53.3	55.3
STAR [54]	2.32	11.69	2.24	1.58	0.98	4.76	3.24	60.5	36.2	58.4	60.9	62.2	53.8	55.1
LDEQ [28]	2.48	12.58	1.59	2.29	1.94	5.36	2.84	62.4	37.3	61.4	63.1	63.1	55.2	57.4
Ours	1.76	8.28	1.27	1.29	1.94	3.80	2.07	63.7	40.1	62.6	64.7	64.7	57.1	58.6

Table 2. FR₁₀ and AUC₁₀ on the WFLW test set. The **best** and **second** best results are marked in colors of red and blue, respectively. The results demonstrate the robustness and effectiveness of our proposed model.

is capable of capturing the contextual features of images and the intrinsic relationships between landmarks.

By exploring the relationships between bases in the heatmap space to model the underlying geometric relations

among landmarks, our method achieves a significant improvement of 0.49 in NME on the COFW dataset, which contains heavy occlusions and a wide range of head poses, compared to the previous SOTA baseline, STAR [54].

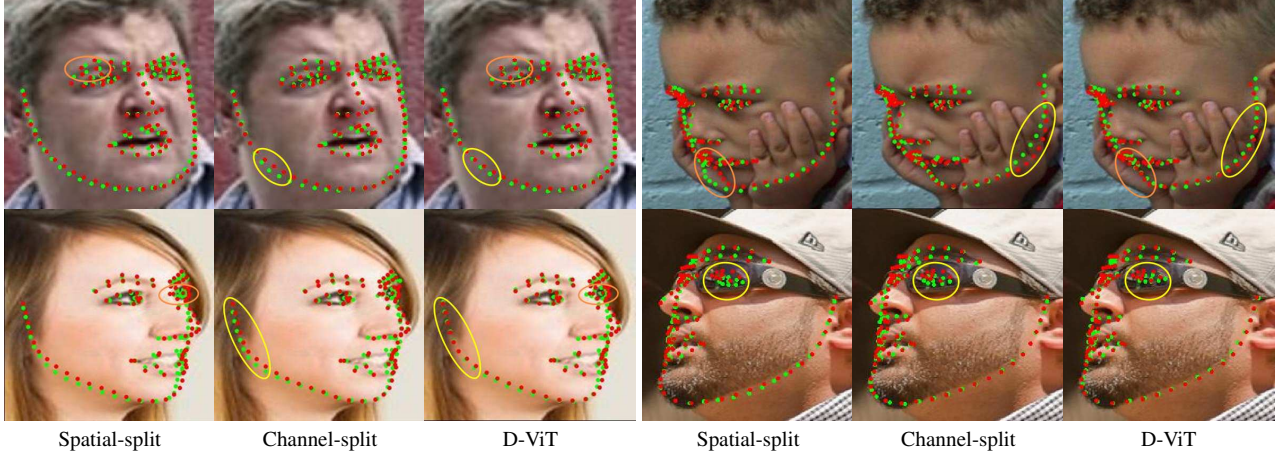


Figure 4. Qualitative results of different prediction blocks on WFLW dataset. Green and red points represent the predicted and ground-truth landmarks, respectively. Orange or Yellow circles indicate the clear failures, which can be improved with help of D-ViT.

Dataset	Connection Strategy			Block Name		
	ResCBSP	DenC	LSC	Spatial-split	Channel-split	D-ViT
COFW	4.14	4.14	4.13	4.18	4.20	4.13
300W	2.89	2.90	2.85	2.87	2.96	2.85

Table 3. Comparisons of different connection strategies and different prediction blocks on dataset COFW and 300W by using 8 prediction blocks. NME scores are reported.

Moreover, our approach also achieves the lowest NME on the full 300W test set.

The FR₁₀ and AUC₁₀ scores on the WFLW dataset, as reported in Tab. 2, demonstrate the robustness and effectiveness of our proposed model. Specifically, our method outperforms previous state-of-the-art methods [28, 31] by 0.32 and 1.30 in FR₁₀ and AUC₁₀, respectively.

4.3. Ablation Studies

In this section, various ablation studies are conducted to verify the specific design decisions in our model architecture. Discussion about the selections of hyper parameters is also included.

D-ViT. Our Dual Vision Transformer (D-ViT) utilizes two types of Vision Transformers (ViTs), specifically the spatial-split ViT and channel-split ViT, to extract spatial features from images and underlying geometric features among landmarks, respectively. To demonstrate the necessity of incorporating the channel-split ViT for exploring the relationships between heatmap bases, we report in Tab. 4a the performance on the WFLW dataset when using spatial-split ViT, channel-split ViT, and our proposed D-ViT separately to construct the prediction blocks. Additionally, Tab. 3 presents the NME performance of different prediction blocks on the COFW and 300W datasets. From the two tables, it can be observed that by incorporating the less effective channel-split ViT to construct D-ViT actually

leads to more accurate detection. This indicates that exploring relationships among heatmap bases has a positive effect on enhancing accurate predictions. Fig. 4 shows some qualitative visualizations. With the help of D-ViT, our model is able to accurately detect landmarks in various scenarios, such as occlusion, expression, blur, and large pose.

Block Name	NME(\downarrow)	FR ₁₀ (\downarrow)	AUC ₁₀ (\uparrow)
Spatial-Split	3.82	2.08	63.2
Channel-Split	3.87	2.36	63.2
D-ViT	3.75	1.76	63.7

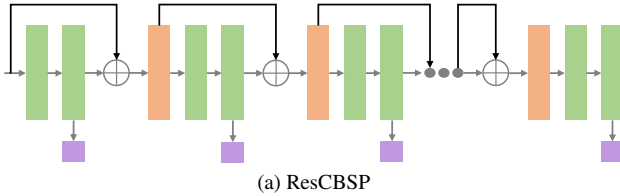
(a) Quantitative comparison of different prediction blocks.

Conn. Strategy	NME(\downarrow)	FR ₁₀ (\downarrow)	AUC ₁₀ (\uparrow)
ResCBSP	3.82	2.16	63.2
DenC	3.81	2.16	63.2
LSC	3.75	1.76	63.7

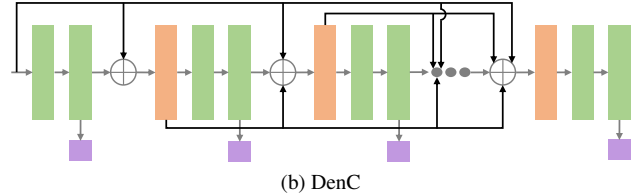
(b) Quantitative comparison of different connection strategies.

Table 4. Comparison results of different prediction blocks (a) and different connection strategies (b) with 8 prediction blocks on WFLW dataset.

Long Skip Connection. Connection strategies for prediction blocks are typically either residual connections between sequential predictions (ResCBSP) [16] or



(a) ResCBSP



(b) DenC

Figure 5. Illustrations of alternative skip connections. ResCBSP denotes the residual connections between two sequential prediction blocks. DenC denotes dense connections where any two prediction blocks have a skip connection. Refer to Fig. 1 for definition of prediction block and colorful rectangles.

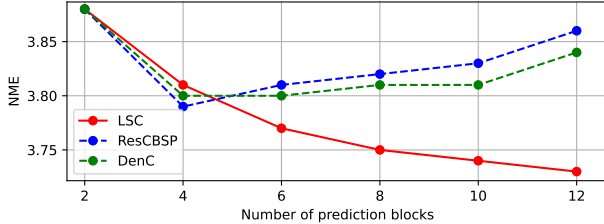


Figure 6. NME against number of prediction blocks on WFLW dataset. When the number is 2, three strategies essentially represent the same structure. When the number exceeds 4, the performance of ResCBSP or DenC starts to get worse. While with our proposed LSC, the model can benefit from a deeper architecture.

dense connections (DenC) [17], as illustrated in Fig. 5a and Fig. 5b. Besides, residual connections are commonly used in stacked Hourglasses (HGs) networks [29, 52], which often serve as backbones for facial landmark detection [18, 21, 29, 44, 54]. However, Fig. 6 indicates that using these two strategies to connect prediction blocks built on ViTs results in diminished performance as the number of blocks increases. This is because intermediate supervision can lead to the loss of useful information. To address this, we propose using long skip connections (LSC) to distribute low-level image features from ResNet to each prediction block, thereby making deeper network architectures feasible. Additionally, the quantitative comparison of different connection strategies with 8 prediction blocks reported in Tab. 4b on the WFLW dataset, along with the results in Tab. 3 on the COFW and 300W datasets, both demonstrate the superior effectiveness of our proposed LSC.

Cross-dataset Validations. To further validate our design decisions, we conduct a cross-dataset validation experiment that includes quantitative comparisons of different prediction blocks and connection strategies, similar to the one described in Tab. 4. However, different from that experiment, we train the models on the WFLW dataset and evaluate them on subsets of the WFLW-V dataset, *i.e.*, the easy set and the hard set. The results reported in Tab. 5 indicate that our proposed D-ViT and LSP still achieve the best NME score in the cross-dataset validations, demonstrating superior generalization.

Weight for Intermediate Supervision. Weight w in Eq. (6) is a balance between multiple intermediate su-

Block Name	Easy	Hard
Spatial-split	1.74	2.96
Channel-split	1.69	3.12
D-ViT	1.66	2.91

(a) Quantitative comparison of different prediction blocks.

Connection Strategy	Easy	Hard
ResCBSP	1.77	3.12
DenC	1.74	3.06
LSC	1.66	2.91

(b) Quantitative comparison of different connection strategies.

Table 5. Cross-dataset Validations. We train all models on WFLW dataset, and report NME on the two subsets of WFLW-V dataset. The results further demonstrate the effectiveness of our design.

w	1.0	1.2	1.4	1.6
NME(\downarrow)	3.78	3.75	3.77	3.77

Table 6. Analysis of weight w in Eq. (6). We report NME scores with varying w on WFLW dataset.

pervisions. To study the influence, we carried out experiments with w ranging from 1.0 to 1.6, as shown in Tab. 6. Our model achieves the best performance with w set to 1.2. Thus, we choose 1.2 as the default setting.

5. Conclusion

This paper introduces a new approach for facial landmark detection based on our proposed dual vision transformers, which extract image features through spatial-split features and learn inherent geometric relations through channel-split features. Extensive experiments demonstrate that D-ViT plays an effective role in facial landmark detection, achieving new state-of-the-art performance on three benchmarks. Additionally, various ablation studies are conducted to demonstrate the necessity of the design choices in our network. Moreover, we also investigate the effect of different connection strategies between prediction blocks, revealing that our proposed long skip connection allows the network to incorporate more prediction blocks to improve accuracy without losing useful features in deeper blocks.

References

[1] Shaojie Bai, J. Zico Kolter, and Vladlen Koltun. Deep equilibrium models. In *Advances in Neural Information Processing Systems (NeurIPS)*, 2019. [2](#)

[2] Adrian Bulat, Enrique Sanchez, and Georgios Tzimiropoulos. Subpixel heatmap regression for facial landmark localization, 2021. [2](#)

[3] Xavier P. Burgos-Artizzu, Pietro Perona, and Piotr Dollar. Robust face landmark estimation under occlusion. In *Proceedings of the IEEE International Conference on Computer Vision (ICCV)*, December 2013. [1, 2, 5](#)

[4] T.F. Cootes, G.J. Edwards, and C.J. Taylor. Active appearance models. *IEEE Transactions on Pattern Analysis and Machine Intelligence*, 23(6):681–685, 2001. [1](#)

[5] Radek Danček, Michael J. Black, and Timo Bolkart. Emoca: Emotion driven monocular face capture and animation. In *Proceedings of the IEEE/CVF Conference on Computer Vision and Pattern Recognition (CVPR)*, pages 20311–20322, June 2022. [1](#)

[6] Arnaud Dapogny, Kevin Bailly, and Matthieu Cord. Decaf: Deep convolutional cascade for face alignment in the wild. In *Proceedings of the IEEE/CVF International Conference on Computer Vision (ICCV)*, October 2019. [1, 2, 6](#)

[7] Jiankang Deng, George Trigeorgis, Yuxiang Zhou, and Stefanos Zafeiriou. Joint multi-view face alignment in the wild. *IEEE Transactions on Image Processing*, 28(7):3636–3648, 2019. [2](#)

[8] Yu Deng, Jiaolong Yang, Sicheng Xu, Dong Chen, Yunde Jia, and Xin Tong. Accurate 3d face reconstruction with weakly-supervised learning: From single image to image set. In *Proceedings of the IEEE/CVF Conference on Computer Vision and Pattern Recognition (CVPR) Workshops*, June 2019. [1](#)

[9] Xuanyi Dong, Yan Yan, Wanli Ouyang, and Yi Yang. Style aggregated network for facial landmark detection. In *Proceedings of the IEEE Conference on Computer Vision and Pattern Recognition (CVPR)*, pages 379–388, 2018. [2](#)

[10] Alexey Dosovitskiy, Lucas Beyer, Alexander Kolesnikov, Dirk Weissenborn, Xiaohua Zhai, Thomas Unterthiner, Mostafa Dehghani, Matthias Minderer, Georg Heigold, Sylvain Gelly, Jakob Uszkoreit, and Neil Houlsby. An image is worth 16x16 words: Transformers for image recognition at scale. *ICLR*, 2021. [1, 3](#)

[11] G.J. Edwards, C.J. Taylor, and T.F. Cootes. Interpreting face images using active appearance models. In *Proceedings Third IEEE International Conference on Automatic Face and Gesture Recognition*, pages 300–305, 1998. [1](#)

[12] Zhen-Hua Feng, Josef Kittler, Muhammad Awais, Patrik Huber, and Xiao-Jun Wu. Wing loss for robust facial landmark localisation with convolutional neural networks. In *Proceedings of the IEEE Conference on Computer Vision and Pattern Recognition (CVPR)*, June 2018. [2, 6](#)

[13] Zheng Gao and Ioannis Patras. Self-supervised facial representation learning with facial region awareness. In *Proceedings of the IEEE/CVF Conference on Computer Vision and Pattern Recognition*, pages 2081–2092, 2024. [2, 6](#)

[14] Tal Hassner, Shai Harel, Eran Paz, and Roee Enbar. Efficient face frontalization in unconstrained images. In *Proceedings of the IEEE conference on computer vision and pattern recognition*, pages 4295–4304, 2015. [1](#)

[15] Kaiming He, Xiangyu Zhang, Shaoqing Ren, and Jian Sun. Deep residual learning for image recognition. In *Proceedings of the IEEE Conference on Computer Vision and Pattern Recognition (CVPR)*, June 2016. [2, 5](#)

[16] Kaiming He, Xiangyu Zhang, Shaoqing Ren, and Jian Sun. Deep residual learning for image recognition. In *Proceedings of the IEEE conference on computer vision and pattern recognition*, pages 770–778, 2016. [7](#)

[17] Gao Huang, Zhuang Liu, Laurens Van Der Maaten, and Kilian Q Weinberger. Densely connected convolutional networks. In *Proceedings of the IEEE conference on computer vision and pattern recognition*, pages 4700–4708, 2017. [8](#)

[18] Yangyu Huang, Hao Yang, Chong Li, Jongyoo Kim, and Fangyun Wei. Adnet: Leveraging error-bias towards normal direction in face alignment. In *Proceedings of the IEEE/CVF International Conference on Computer Vision*, pages 3080–3090, 2021. [1, 2, 4, 6, 8](#)

[19] Kazemi and Sullivan. One millisecond face alignment with an ensemble of regression trees. *PROC CVPR IEEE*, 2014. [1](#)

[20] Abhinav Kumar, Tim K. Marks, Wenxuan Mou, Ye Wang, Michael Jones, Anoop Cherian, Toshiaki Koike-Akino, Xiaoming Liu, and Chen Feng. Luvli face alignment: Estimating landmarks’ location, uncertainty, and visibility likelihood. In *IEEE/CVF Conference on Computer Vision and Pattern Recognition (CVPR)*, 2020. [2, 6](#)

[21] Xing Lan, Qinghao Hu, and Jian Cheng. HIH: towards more accurate face alignment via heatmap in heatmap. *CoRR*, abs/2104.03100, 2021. [1, 2, 4, 5, 6, 8](#)

[22] Chunlu Li, Andreas Morel-Forster, Thomas Vetter, Bernhard Egger, and Adam Kortylewski. Robust model-based face reconstruction through weakly-supervised outlier segmentation. In *Proceedings of the IEEE/CVF Conference on Computer Vision and Pattern Recognition*, pages 372–381, 2023. [1](#)

[23] H. Li, Z. Guo, S. Rhee, S. Han, and J. Han. Towards accurate facial landmark detection via cascaded transformers. In *2022 IEEE/CVF Conference on Computer Vision and Pattern Recognition (CVPR)*, pages 4166–4175, Los Alamitos, CA, USA, jun 2022. IEEE Computer Society. [1, 2, 5, 6](#)

[24] Weijian Li, Yuhang Lu, Kang Zheng, Haofu Liao, Chihung Lin, Jiebo Luo, Chi-Tung Cheng, Jing Xiao, Le Lu, Chang-Fu Kuo, and Shun Miao. Structured landmark detection via topology-adapting deep graph learning. In *European Conference on Computer Vision*, 2020. [1, 2, 6](#)

[25] Chunze Lin, Beier Zhu, Quan Wang, Renjie Liao, Chen Qian, Jiwen Lu, and Jie Zhou. Structure-coherent deep feature learning for robust face alignment. *IEEE Transactions on Image Processing*, 30:5313–5326, 2021. [1, 2](#)

[26] Rosanne Liu, Joel Lehman, Piero Molino, Felipe Petroski Such, Eric Frank, Alexander Sergeev, and Jason Yosinski. An intriguing failing of convolutional neural networks and the coordconv solution. *ArXiv*, abs/1807.03247, 2018. [2](#)

[27] Jiangjing Lv, Xiaohu Shao, Junliang Xing, Cheng Cheng, and Xi Zhou. A deep regression architecture with two-stage re-initialization for high performance facial landmark detection. In *Proceedings of the IEEE Conference on Computer Vision and Pattern Recognition (CVPR)*, July 2017. 2

[28] Paul Micaelli, Arash Vahdat, Hongxu Yin, Jan Kautz, and Pavlo Molchanov. Recurrence without recurrence: Stable video landmark detection with deep equilibrium models. In *Proceedings of the IEEE/CVF Conference on Computer Vision and Pattern Recognition (CVPR)*, pages 22814–22825, June 2023. 2, 5, 6, 7

[29] Alejandro Newell, Kaiyu Yang, and Jia Deng. Stacked hourglass networks for human pose estimation. In *European Conference on Computer Vision*, 2016. 2, 4, 8

[30] Aiden Nibali, Zhen He, Stuart Morgan, and Luke A. Pendergast. Numerical coordinate regression with convolutional neural networks. *CoRR*, abs/1801.07372, 2018. 2

[31] Andrés Prados-Torreblanca, José M Buenaposada, and Luis Baumela. Shape preserving facial landmarks with graph attention networks. In *33rd British Machine Vision Conference 2022, BMVC 2022, London, UK, November 21-24, 2022*. BMVA Press, 2022. 1, 2, 6, 7

[32] Shengju Qian, Keqiang Sun, Wayne Wu, Chen Qian, and Jiaya Jia. Aggregation via separation: Boosting facial landmark detector with semi-supervised style translation. In *Proceedings of the IEEE/CVF International Conference on Computer Vision*, pages 10153–10163, 2019. 6

[33] O. Ronneberger, P. Fischer, and T. Brox. U-net: Convolutional networks for biomedical image segmentation. In *Medical Image Computing and Computer-Assisted Intervention (MICCAI)*, volume 9351 of *LNCS*, pages 234–241. Springer, 2015. (available on arXiv:1505.04597 [cs.CV]). 2

[34] Christos Sagonas, Georgios Tzimiropoulos, Stefanos Zafeiriou, and Maja Pantic. 300 faces in-the-wild challenge: The first facial landmark localization challenge. In *Proceedings of the IEEE International Conference on Computer Vision (ICCV) Workshops*, June 2013. 1, 2, 5

[35] Wenzhe Shi, Jose Caballero, Ferenc Huszár, Johannes Totz, Andrew P. Aitken, Rob Bishop, Daniel Rueckert, and Zehan Wang. Real-time single image and video super-resolution using an efficient sub-pixel convolutional neural network. In *2016 IEEE Conference on Computer Vision and Pattern Recognition (CVPR)*, pages 1874–1883, 2016. 5

[36] Brandon M. Smith, Li Zhang, Jonathan Brandt, Zhe Lin, and Jianchao Yang. Exemplar-based face parsing. In *Proceedings of the IEEE Conference on Computer Vision and Pattern Recognition (CVPR)*, June 2013. 1

[37] Ke Sun, Bin Xiao, Dong Liu, and Jingdong Wang. Deep high-resolution representation learning for human pose estimation. In *CVPR*, 2019. 2, 6

[38] Yi Sun, Xiaogang Wang, and Xiaoou Tang. Deep convolutional network cascade for facial point detection. In *Proceedings of the IEEE Conference on Computer Vision and Pattern Recognition (CVPR)*, June 2013. 1, 2

[39] Jonathan J Tompson, Arjun Jain, Yann LeCun, and Christoph Bregler. Joint training of a convolutional network and a graphical model for human pose estimation. In Z. Ghahra-
mani, M. Welling, C. Cortes, N. Lawrence, and K.Q. Weinberger, editors, *Advances in Neural Information Processing Systems*, volume 27. Curran Associates, Inc., 2014. 2

[40] George Trigeorgis, Patrick Snape, Mihalis A. Nicolaou, Epameinondas Antonakos, and Stefanos Zafeiriou. Mnemonic descent method: A recurrent process applied for end-to-end face alignment. In *Proceedings of the IEEE Conference on Computer Vision and Pattern Recognition (CVPR)*, June 2016. 2

[41] Ashish Vaswani, Noam Shazeer, Niki Parmar, Jakob Uszkoreit, Llion Jones, Aidan N Gomez, Łukasz Kaiser, and Illia Polosukhin. Attention is all you need. In I. Guyon, U. Von Luxburg, S. Bengio, H. Wallach, R. Fergus, S. Vishwanathan, and R. Garnett, editors, *Advances in Neural Information Processing Systems*, volume 30. Curran Associates, Inc., 2017. 4

[42] Jingdong Wang, Ke Sun, Tianheng Cheng, Borui Jiang, Chaorui Deng, Yang Zhao, Dong Liu, Yadong Mu, Mingkui Tan, Xinggang Wang, Wenyu Liu, and Bin Xiao. Deep high-resolution representation learning for visual recognition. *TPAMI*, 2019. 2

[43] Mei Wang and Weihong Deng. Deep face recognition: A survey. *Neurocomputing*, 429:215–244, 2021. 1

[44] Xinyao Wang, Liefeng Bo, and Li Fuxin. Adaptive wing loss for robust face alignment via heatmap regression. In *The IEEE International Conference on Computer Vision (ICCV)*, October 2019. 1, 2, 4, 6, 8

[45] Wayne Wu, Chen Qian, Shuo Yang, Quan Wang, Yici Cai, and Qiang Zhou. Look at boundary: A boundary-aware face alignment algorithm. In *Proceedings of the IEEE Conference on Computer Vision and Pattern Recognition (CVPR)*, June 2018. 1, 2, 5, 6

[46] Jiahao Xia, Weiwei Qu, Wenjian Huang, Jianguo Zhang, Xi Wang, and Min Xu. Sparse local patch transformer for robust face alignment and landmarks inherent relation learning. In *Proceedings of the IEEE/CVF Conference on Computer Vision and Pattern Recognition (CVPR)*, pages 4052–4061, June 2022. 1, 2, 5, 6

[47] Heng Yang, Wenxuan Mou, Yichi Zhang, Ioannis Patras, Hatice Gunes, and Peter Robinson. Face alignment assisted by head pose estimation. *Computer Science*, 7, 2015. 1

[48] Shuo Yang, Ping Luo, Chen-Change Loy, and Xiaoou Tang. Wider face: A face detection benchmark. In *Proceedings of the IEEE Conference on Computer Vision and Pattern Recognition (CVPR)*, June 2016. 5

[49] Sen Yang, Zhibin Quan, Mu Nie, and Wankou Yang. Transpose: Keypoint localization via transformer. In *IEEE/CVF International Conference on Computer Vision (ICCV)*, 2021. 1

[50] Feng Zhang, Xiatian Zhu, Hanbin Dai, Mao Ye, and Ce Zhu. Distribution-aware coordinate representation for human pose estimation. In *IEEE/CVF Conference on Computer Vision and Pattern Recognition (CVPR)*, June 2020. 5

[51] Yizhe Zhang, Ming Shao, Edward K. Wong, and Yun Fu. Random faces guided sparse many-to-one encoder for pose-invariant face recognition. In *IEEE International Conference on Computer Vision*, 2013. 1

- [52] Zhanpeng Zhang, Ping Luo, Chen Change Loy, and Xiaoou Tang. Facial landmark detection by deep multi-task learning. In *Computer Vision–ECCV 2014: 13th European Conference, Zurich, Switzerland, September 6–12, 2014, Proceedings, Part VI* 13, pages 94–108. Springer, 2014. [4](#), [8](#)
- [53] Erjin Zhou, Haoqiang Fan, Zhimin Cao, Yuning Jiang, and Qi Yin. Extensive facial landmark localization with coarse-to-fine convolutional network cascade. In *Proceedings of the IEEE International Conference on Computer Vision (ICCV) Workshops*, June 2013. [1](#), [2](#)
- [54] Zhenglin Zhou, Huaxia Li, Hong Liu, Nanyang Wang, Gang Yu, and Rongrong Ji. Star loss: Reducing semantic ambiguity in facial landmark detection. In *Proceedings of the IEEE/CVF Conference on Computer Vision and Pattern Recognition (CVPR)*, pages 15475–15484, June 2023. [1](#), [2](#), [4](#), [5](#), [6](#), [8](#)
- [55] Shizhan Zhu, Cheng Li, Chen Change Loy, and Xiaoou Tang. Face alignment by coarse-to-fine shape searching. In *Proceedings of the IEEE Conference on Computer Vision and Pattern Recognition (CVPR)*, June 2015. [1](#), [2](#)
- [56] Xiangyu Zhu, Zhen Lei, Junjie Yan, Dong Yi, and Stan Z. Li. High-fidelity pose and expression normalization for face recognition in the wild. In *Proceedings of the IEEE Conference on Computer Vision and Pattern Recognition (CVPR)*, June 2015. [1](#)

Cascaded Dual Vision Transformer for Accurate Facial Landmark Detection

Technical Appendix

In this supplementary material, we provide more details and results omitted from the main paper for brevity. Specifically, in Sec. A, we introduce the GPU memory requirement; in Sec. B, we compare our method by training and testing networks with similar computational capacity; in Sec. C, we investigate the impact of input image resolution; and in Sec. D, we present visual comparisons on the COFW and 300W datasets.

A. GPU Memory Requirement

In Tab. S1, we report the memory required for each GPU during training, as well as the number of parameters for different numbers of prediction blocks.

#Pred. Blocks	2	4	6	8	10	12
Memory (GB)	4.4	6.3	8.2	10.3	12.1	14.2
#Param. (M)	24.4	48.4	72.4	96.4	120.4	144.4

Table S1. Memory required for each GPU during training, and number of parameters for different numbers of prediction blocks.

B. Comparison on Similar Compute Capacity

Our proposed Long Skip Connection avoid losing useful information due to intermediate supervision and make deeper network architectures feasible. However, improved performance is not solely attributed to increased computational capacity. When we use 4 prediction blocks and reduce the dimension of the feature maps to (160, 32, 32), the number of parameters in our network is comparable to other baselines. As reported in Tab. S2, the NME score still surpasses the previous SOTA method LDEQ [2] by 0.08, indicating the effectiveness of our proposed architecture.

C. Comparison on Different Image Resolutions

We investigate the influence of different input image resolutions, as shown in Fig. S1. Specifically, D-ViT improves the performance by 0.09, 0.08 and 0.07 at resolutions of 64px, 128px, and 256px, respectively, indicating that our proposed method is not sensitive to the input image size.

Method	#Param. (M)	NME(\downarrow)	FR ₁₀ (\downarrow)	AUC ₁₀ (\uparrow)
HIH [1]	22.7	4.08	2.60	60.5
SPIGA [3]	60.3	4.06	2.08	60.6
STAR [4]	13.4	4.02	2.32	60.5
LDEQ [2]	21.8	3.92	2.48	62.4
Ours_nstack4	21.0	3.84	2.44	63.3

Table S2. Comparisons on WFLW dataset. We reduce the number of network parameters to 21M, denoted as “Ours_nstack4”. Our proposed method still shows effectiveness.

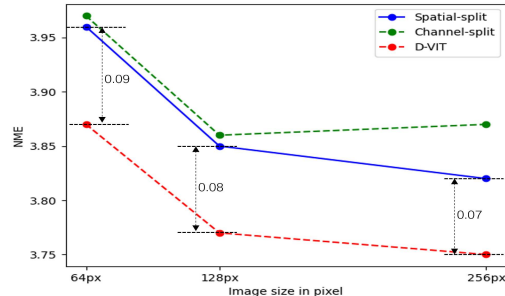


Figure S1. NME against different input image sizes on WFLW dataset.

D. Visual Results on COFW and 300W

In this section, we present the qualitative comparison results on COFW and 300W. Fig. S3 and Fig. S2 show the results of different prediction blocks. Fig. S4 and Fig. S5 show the comparisons of different skip connection strategies. With the help of our proposed D-ViT and LSC, the detection accuracy for landmarks is improved.

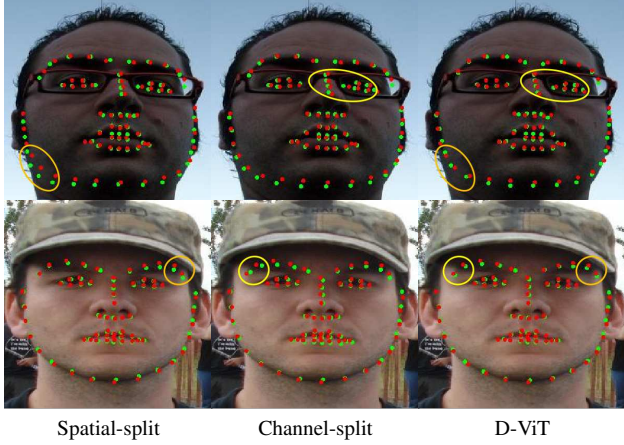


Figure S2. Visual comparison of different prediction blocks on 300W. Green and red points represent the predicted and ground-truth landmarks, respectively.

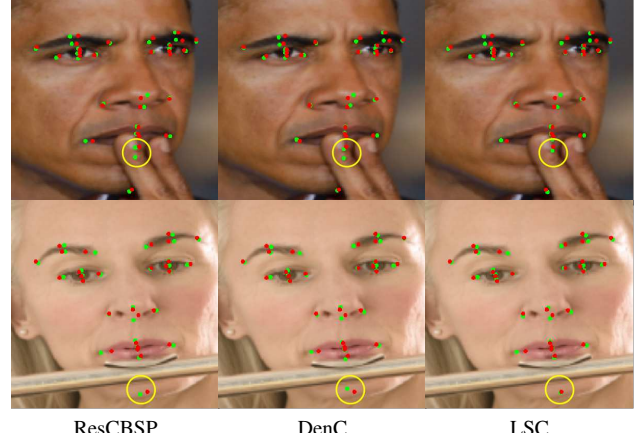


Figure S4. Qualitative results of different skip connection strategies on COFW by using 8 prediction blocks. Green and red points represent the predicted and ground-truth landmarks, respectively.

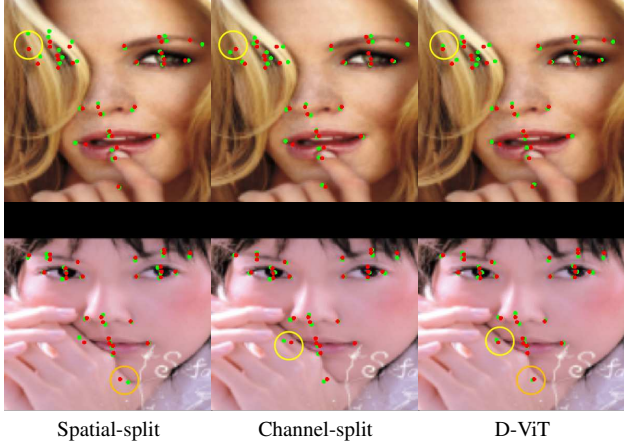


Figure S3. Visual results on the COFW dataset which contains heavy occlusions. Geometric relations among landmarks play a crucial role in accurately predicting landmarks on occluded parts (indicated by orange and yellow circles). Our D-ViT captures both semantic image features and the underlying geometric features among landmarks, enabling our model to make more accurate predictions even in the presence of occlusions.

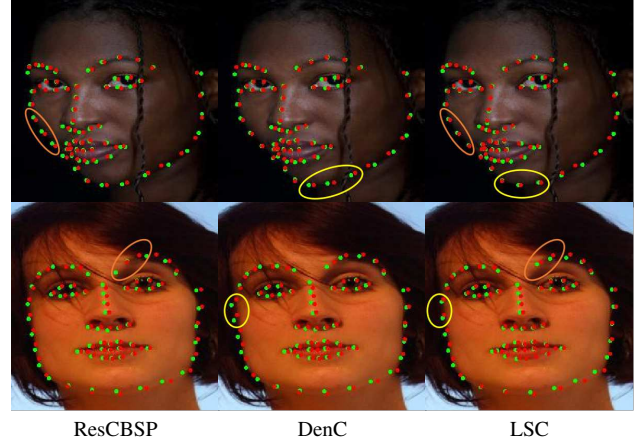


Figure S5. Qualitative results of different skip connection strategies on 300W by using 8 prediction blocks. Green and red points represent the predicted and ground-truth landmarks, respectively.

References

- [1] Xing Lan, Qinghao Hu, and Jian Cheng. HIH: towards more accurate face alignment via heatmap in heatmap. *CoRR*, abs/2104.03100, 2021. [1](#)
- [2] Paul Micaelli, Arash Vahdat, Hongxu Yin, Jan Kautz, and Pavlo Molchanov. Recurrence without recurrence: Stable video landmark detection with deep equilibrium models. In *Proceedings of the IEEE/CVF Conference on Computer Vision and Pattern Recognition (CVPR)*, pages 22814–22825, June 2023. [1](#)
- [3] Andrés Prados-Torreblanca, José M Buenaposada, and Luis Baumela. Shape preserving facial landmarks with graph attention networks. In *33rd British Machine Vision Conference 2022, BMVC 2022, London, UK, November 21-24, 2022*. BMVA Press, 2022. [1](#)
- [4] Zhenglin Zhou, Huaxia Li, Hong Liu, Nanyang Wang, Gang Yu, and Rongrong Ji. Star loss: Reducing semantic ambiguity in facial landmark detection. In *Proceedings of the IEEE/CVF Conference on Computer Vision and Pattern Recognition (CVPR)*, pages 15475–15484, June 2023. [1](#)